#### A multi-scale computer model of mechanical ventilation for COVID-19 patients

Shea Middleton<sup>1</sup>, Elizabeth Dimbath<sup>1</sup>, Veeranna Maddipati<sup>4</sup>, MD, M. Sean Peach<sup>3</sup>, MD, PhD, Andrew W. Ju<sup>3</sup>, MD, Stephanie George<sup>3</sup>, PhD, Alex Vadati, PhD<sup>2\*</sup>

<sup>1</sup>Department of Biomedical Engineering, Pratt School of Engineering, Duke University, Durham, NC, USA

<sup>2</sup>Department of Engineering, College of Engineering and Technology, East Carolina University, Greenville, NC, USA

<sup>3</sup>Department of Radiation Oncology, Brody School of Medicine, East Carolina University, Greenville, NC, USA

<sup>4</sup>Division of Pulmonary and Critical Medicine, Brody School of Medicine, East Carolina University, Greenville, NC, USA

## **Corresponding Author:**

\*Alex Vadati, PhD

Email: vahdatia18@ecu.edu Telephone: 252-737-7779

Address: Ross Hall, East Carolina University, Greenville, NC, USA

**Abstract:** There is a need for more individualized treatment of critically ill patients receiving mechanical ventilation (MV). Therefore, this research aims to create a preliminary multi-scale computational modeling framework for MV in critically ill COVID-19 patients as a step toward studying region-specific and overall lung dynamics in these patients. This goal was accomplished by developing proof-of-concept image-based computer models providing insight into airflow redistribution and volume and pressure gradients on a lobe-specific basis. Our *in silico* multi-scale MV models simulated redistribution of ventilation for up to 20% of air volume from severely damaged lung lobes to the lobes less affected by COVID-19, hence potentially revealing a risk factor of MV-induced volutrauma due to heterogeneity of lung damage distribution in COVID-19. This study lays the foundation for future COVID-19 patient-specific lung models for individualized simulation of MV.

**Keywords:** Pulmonary biomechanics, COVID-19, Pulmonary ventilation, Computer modeling, Lung mechanics, Mechanical ventilation

### 1. Introduction

Coronavirus disease-2019 (COVID-19) is a highly transmissible disease caused by a coronavirus known as severe acute respiratory syndrome coronavirus-2 (SARS-CoV-2) that typlically attacks the lung in a manner showing similarities to acute respiratory distress syndrome (ARDS) [1]. Despite the development and distribution of COVID-19 vaccines, consistently developing new variants highlight the continued need for novel methods to understand and treat COVID-19 [1]–[3].

COVID-19 can give rise to COVID-19 ARDS (CARDS), defined by pulmonary edema with diffuse alveolar damage (DAD), affecting both lung compliance and the number of alveoli available to participate in gas exchange. There are pronounced differences between the symptomology of CARDS and typical ARDS. CARDS tend to have worse outcomes than typical ARDS with typical ARDS having a mortality rate of 35.3% to 40.0% for intensive care unit (ICU) and hospital stays, while CARDS mortality has been reported to be between 26% and 61.5% [4]. Imaging of CARDS has shown unique features, including the increased peripheral occurrence of consolidation, higher occurrence of ground-glass opacities (GGOs), lower lung predominance, the appearance of more rounded opacities, and increased vascular thickening [4]. At the microscale, although COVID-19 exhibits DAD similar to that of typical ARDS, COVID-19 also shows extensive microangiopathy (damage to small blood vessels) that differentiates it from other lung pathologies [5].

COVID-19 patients with respiratory failure are often treated with mechanical ventilation (MV) in an intensive care unit (ICU) due to either inadequate oxygenation or help needed with the work of breathing [6]. This invasive procedure carries the risk of ventilator-induced lung injury (VILI), often due to physiologically-incompatible positive pressure configuration leading to high volumetric strain gradients and localized damage in the lung [7]. Moreover, VILI may contribute to the high mortality rate of COVID-19 patients subjected to MV, with a meta-analysis of 57,420 COVID-19 patients that received MV reporting a case fatality rate of 45% that increased with age [8]. Therefore, understanding the interaction between CARDS lungs and MV is essential.

Mathematical and computational models can be used to assess the results of MV and test novel MV protocols. Additionally, in silico modeling of the lung can enable greater control of MV parameters than in vitro or cadaver modeling. A recent systematic literature review by Warnaar et al. [9] found 149 publications on computational physiological modeling of MV, out of which 131 articles modeled lung mechanics. For instance, E. Dincel [10] presented a comprehensive overview of in silico MV models by examining and designing algorithms for various advanced MV modes, demonstrating the great potential of MV simulations to simulate variable ventilation conditions, as further exemplified by the work of Das et al. [11] to examine differences in CARDS and other lung pathologies when exposed to different ventilation parameters. In another approach, a virtual patient model created by Morton et al. [12] was used to predict the response of mechanically ventilated lung based on clinical data from an MV study by Szlavecz et al. [13]. However, neither Das et al. [11] nor Morton et al.'s [12] pioneering studies were image-based. Image-based computer models can offer a more patient-specific approach to simulate fluid dynamics and tissue mechanics of diseased, and mechanically ventilated lungs. Such image-based approaches to creating computer models of lung can serve a wide variety of purposes, including multi-scale simulation of gas flow and ventilation [14]-[18] as well as MV dynamics [10], [12], [19], [20]. However, there are few image-based modeling studies of COVID-19 lungs, as is expected for a relatively recent disease [11]. Nonetheless, a strong foundation for future COVID-19 lung models can be built using existing lung models and image-based methodologies. An example image-based study is a computational fluid dynamics model developed by Kim & Pidaparti [21] for MV and normal breathing in a simplified CT-based airway geometry. However, this study forgoes patient-specificity of the lung geometry. Hence, there is a need of image-based MV computer models, particularly for COVID-19, in the research literature.

This study aims to present a preliminary *in silico* model for simulating patient-specific responses to MV, based on clinically sourced CT images of COVID-19-afflicted lungs. The model couples 16 generations of airways to a mathematical (zero-dimensional) acinar model that includes alveolar mechanics. A major assumption of this modeling study is that the GGO and consolidation regions show increased stiffness compared to heatlhy regions, and that the increased stiffness can be modeled using a modified pressure-volume relationship for the acini of the lung. The study rests on the hypothesis that the subject's lung and lobar geometry are a major determiant of the lung's response to MV. This model subsequently gives insight into potential risk factors of VILI, and sets a foundation for future personalized treatment strategies.

## 2. Methods

# 2.1 Imaging

The East Carolina University University and Medical Center Institutional Review Board (UMCIRB) approved the image collection and processing methodology used in this study with study ID 20-001447. Four patients recently hospitalized for advanced cases of COVID-19 at Vidant Medical Center (Greenville, North Carolina, USA) were imaged using four-dimensional computed tomography (4DCT) scanning during tidal breathing using an Optima CT580 RT scanner (GE Healthcare, Waukesha, WI). Informed consent was obtained from each patient. A Varian 4DCT Real-time Position Management system (Varian Medical Systems, Palo Alto, CA) captured the patient's real-time external chest motion amplitude, and Advantage 4D (GE Healthcare, Waukesha, WI) software retrospectively assigned the CT data into corresponding phases of the respiratory cycle. CT imaging parameters consisted of 120 kVp, 300 mAs, and 20 mm collimation.

Patient data retrieved include age, height, weight, smoking status, and sex, as shown in Table 1. Each patient was a male non-smoker.

Subject	Age	Weight (kg)	Height (m)	BMI	Predicted body
Number					weight (PBW) (kg)
1	51	88.5	1.676	31.4	63.756
2	67	110.2	1.727	36.8	68.372
3	63	90.7	1.524	39.3	50.000
4	75	95.3	1.829	28.5	77.603
Average	64	96.2	1.689	34.0	64.933

Table 1: COVID-19 subject demographics.

# 2.2 Airway and Lobe Segmentation

The major airways of each subject were segmented from the end-inspiratory phase using Materialise Mimics 23.0 (Materialise NV, Belgium). This method generated the first five to six generations. Centerline detection and extraction of segmented major airways were also performed using Mimics 23.0, as described in Bordas et al.'s work [22]. Finally, the geometry of each lobe was segmented at the end-inspiratory and end-

expiratory phases using the Chest Imaging Platform [23] available in open source software 3D Slicer [24], [25].

# 2.3 Airway Generation

Patient-specific airway segmentation was constrained beyond the first few generations by CT image resolution. A space-filling airway generation algorithm with random heterogeneity based on the work of Tawhai et al. [26], [27] available in the C++ simulation package CHASTE (Cardiac, Heart, and Soft Tissue Environment) [28], [29] was thus used to generate first 16 generations of lung airways. The number of terminal airways, which were coupled to acini, per lung was approximately 15,000 [30]. The lumen diameter for each one-dimensional line segment was assigned based on the Horsfield number [31], [32]:

$$\log D(x) = (x - Max)\log R_d H + \log D_{Max} \tag{1}$$

where x, D, Max,  $D_{Max}$  represented the current Horsfield order, the airway diameter, the maximum Horsfield order and the maximum diameter, respectively.  $R_dH$  represented the anti-log slope of airway diameter plotted against Horsfield order and was assigned to be 1.15 [31]. A flowchart summarizing the methods of the study is shown in Figure 1.

### 2.4 COVID-19 Region Generation

COVID-19-affected regions were segmented in 3D Slicer using the LungCTAnalyzer [33] extension of the Chest Imaging Platform [23]. Hounsfield unit (HU) thresholds between healthy and diseased portions were determined based on a study by Kassin et al. [34]. Healthy lung regions were defined within the range of -1000 to -650 HU. The preset values for COVID-19 lung analysis in the 3D Slicer Chest Imaging Platform [23] and Lung CT Analyzer [33] were thus used to differentiate COVID-19 regions, with voxels in the -650 to -451 HU range treated as GGO and -450 to 0 HU treated as consolidated regions [22]. These COVID-19 regions were then exported to Materialise 3-Matic 16.0 (Materialise NV, Belgium) for post-processing and mesh generation. The 3D STL mesh was used to determine the location (i.e. coordinate points) of the aerated, GGO and consolidated regions. Next, a custom MATLAB (Mathworks Inc, Nautick, USA) script was written to compare the location of each acinus in the airway model with the location of GGO and consolidation regions in the segmented lung geometry. If the acinus fell within a GGO or consolidated region, then a higher stiffness was assigned to the acinus as described in the next section and in Figure 2.

## 2.5 Computational Model Generation

There is considerable debate on whether volume- or pressure-controlled ventilation is more effective [35]. For the purpose of this study, pressure-controlled ventilation was used as it is more readily applicable to the airflow simulation framework in our modeling workflow. Each simulation had an input pressure assigned to the uppermost node in the airway tree to act as the output of an invasively inserted endotracheal tube. The pressure applied here was assigned to atmospheric pressure at the beginning of each simulation to allow time for passive aeration of the lung. Subsequently, the pressure was varied

according to a simulated ventilator waveform. There are a number of important considerations for the simulation of MV, including tidal volume, respiratory rate, inspiratory-to-expiratory ratio (I:E), driving pressure, peak inspiratory pressure (PIP), and positive end-expiratory pressure (PEEP) [36]. Respiratory mechanics during MV is generally estimated using Equation 2 [37], known as the single-compartment MV model:

$$P_V + P_m = \dot{V}_I R_{aw} + \frac{V_T}{C_{RS}} + PEEP \tag{2}$$

where  $P_V$  is the applied ventilator pressure,  $P_m$  is pressure generated by inspiratory muscles,  $\dot{V}_I$  is inspiratory flow,  $R_{aw}$  is airway resistance,  $V_T$  is tidal volume,  $C_{RS}$  is respiratory system compliance, and PEEP is positive end-expiratory pressure [37]. Note that this equation assumes constant values for  $C_{RS}$  and  $R_{aw}$ . For the healthy adult lung  $C_{RS}$  is approximately 50-100 mL/cmH<sub>2</sub>O, and  $R_{aw}$  ranges from 1 to 4 cmH<sub>2</sub>O/L/s [38].

 $P_m$  in Equation 2 is analog to the pleural pressure of the lung for the purpose of the MV modeling framework presented here. We assumed patients were in passive breathing conditions, so there was no rhythmic variation of pleural pressure due to diaphragm movement, unlike natural ventilation. Instead, the ribs, diaphragm, and tissue weighed down the lungs in the supine position. Thus, as lung volume increased, the pleural pressure also increased, so the pleural pressure could become positive at high lung volumes, forcing out excess air. This elastic behavior was conceptualized and modeled by Ismail et al. [16] for the pleural pressure:

$$P_{pl} = P_{pl}^{O} + b_p V_{VCP} + c_p e^{(d_p V_{VCP})}$$
(3)

where  $P_{pl}^O$  is equal to -5 cmH<sub>2</sub>O, and  $b_p$ ,  $c_p$ , and  $d_p$ , are pleural space wall model parameters. These variables suggested by Ismail et al. [16] and fitted to clinical data from Harris et al. [39] were also used here such that  $b_p = 20.344$  cmH<sub>2</sub>O,  $c_p = -33.382$  cmH<sub>2</sub>O, and the unitless parameter  $d_p = -7.686$ , and were assumed to be constant for all patients studied here which means the parameters are not patient-specific. In equation 3, V<sub>VCP</sub> is the percentile vital capacitance and is dependent on patient-specific lung characteristics such that:

$$V_{VCP} = \frac{V - RV}{TLC - RV} \tag{4}$$

where V is the current volume, RV is the residual volume, and TLC is the total lung capacity in liters [16]. The following equations from Boren et al. [40] were used to estimate lung capacities and volumes for each subject:

$$TLC = 0.078H - 7.30 (5)$$

$$RV = 0.019H + 0.0115Ag - 2.24 \tag{6}$$

where H is the subject's height in centimeters, and Ag is the subject's age in years.

The airways of the lung were modeled as a system of rigid pipes with a modified Poiseuille flow following the approach developed by Swan et al. [41] and Ismail et al. [42]. Corrections to the dynamic resistance were applied:

$$Pressure_{inlet} - Pressure_{outlet} = RQ$$
 (7)

$$R = \gamma \left( Re \frac{D_{aw}}{l_{aw}} \right)^{\frac{1}{2}} \left( \frac{8\mu l_{aw}}{\pi (0.5 D_{aw})^4} \right)$$
 (8)

where Q is the flow rate, R is the airway resistance,  $\mu$  is the air dynamic viscosity,  $D_{aw}$  and  $I_{aw}$  are the diameter and length of an airway, respectively,  $R_e$  is the Reynold's number, and  $\gamma$  was set to be generation-dependent based on the work of Ismail et al. [42], [43] and van Ertbruggen et al. [44] as follows:

Generation	0	1	2	3	4	5	6	7	>7
γ	0.162	0.239	0.244	0.295	0.175	0.303	0.356	0.566	0.327

The Reynolds number was defined as:

$$Re = \frac{4\rho|Q|}{\mu \pi D_{aw}} \tag{9}$$

Where  $\rho$  is density of air. All nodal pressures and edge fluxes were solved for simultaneously using multifrontal lower–upper factorization solver UMFPACK [45], [46].

Acinar mechanics were represented with a sigmoidal pressure-volume curve based on the work of Fujioka et al. and Venegas et al. [47], [48]:

$$V_a = A + \frac{B}{1 + e^{-(P_a - C)/D}} \tag{10}$$

where  $V_a$  is the acinar volume,  $P_a$  is the transpulmonary pressure for each acinus, and A, B, C, and D are constants that vary based on surfactant level. Estimated lung volumes of each patient were used to define coefficients A and B, as A is approximated by the residual volume and B is approximated by the vital capacity (see equations 5 and 6). The values of C and D in the sigmoidal model correspond to the inflection point of the curve and were assigned the following values for all patients based on our previous work and Fujioka et al.'s:  $C_{Healthy}$ = 1079 Pa,  $C_{20\%}$ = 1420 Pa,  $C_{60\%}$ = 2359 Pa,  $D_{Healthy}$ = 449 Pa,  $D_{20\%}$ = 451 Pa,  $D_{60\%}$ = 357 Pa. The acini were coupled to each terminus of the generated airway tree. Time-derivative of equation (3) was solved at the end of each terminal bronchiole, where an acinus was connected to an airway, thus coupling the pressure in the airway tree and the acinar model.

GGO and consolidated region volumes created in Section 2.4 were used to identify acinar regions affected by COVID-19. Acini in GGO regions were treated as partially filled with air with 20% reduced surfactant while consolidated regions were treated as mostly occluded with 60% reduced surfactant [49], [50]. Increasing the degree of surfactant reduction corresponded to a decrease in compliance in the acinar mechanics model to represent damage, as shown in Figure 2.

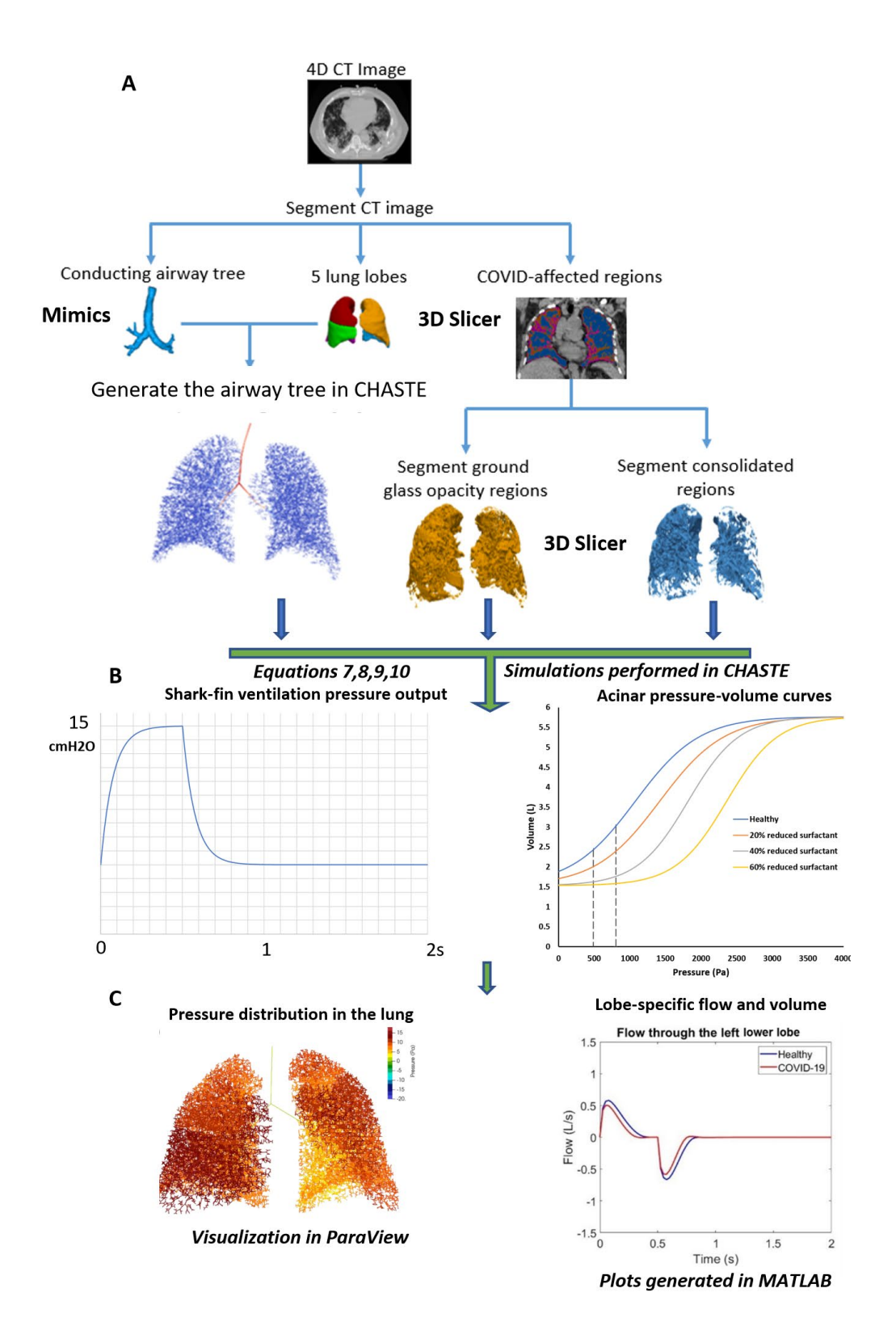


**Figure 1:** Flowchart of the methods employed in the present study, starting with segmentation of lung lobes, infected and healthy regions, and major airways, followed by algorithmic generation of smaller airways (A), and application of mechanical ventilation pressure output at the trachea (B). Acinar mechanics were simulated using sigmoidal pressure-volume relationships (B). The simulations produced air pressure distribution in the lung and lobe-specific flow rate and air volume (C).

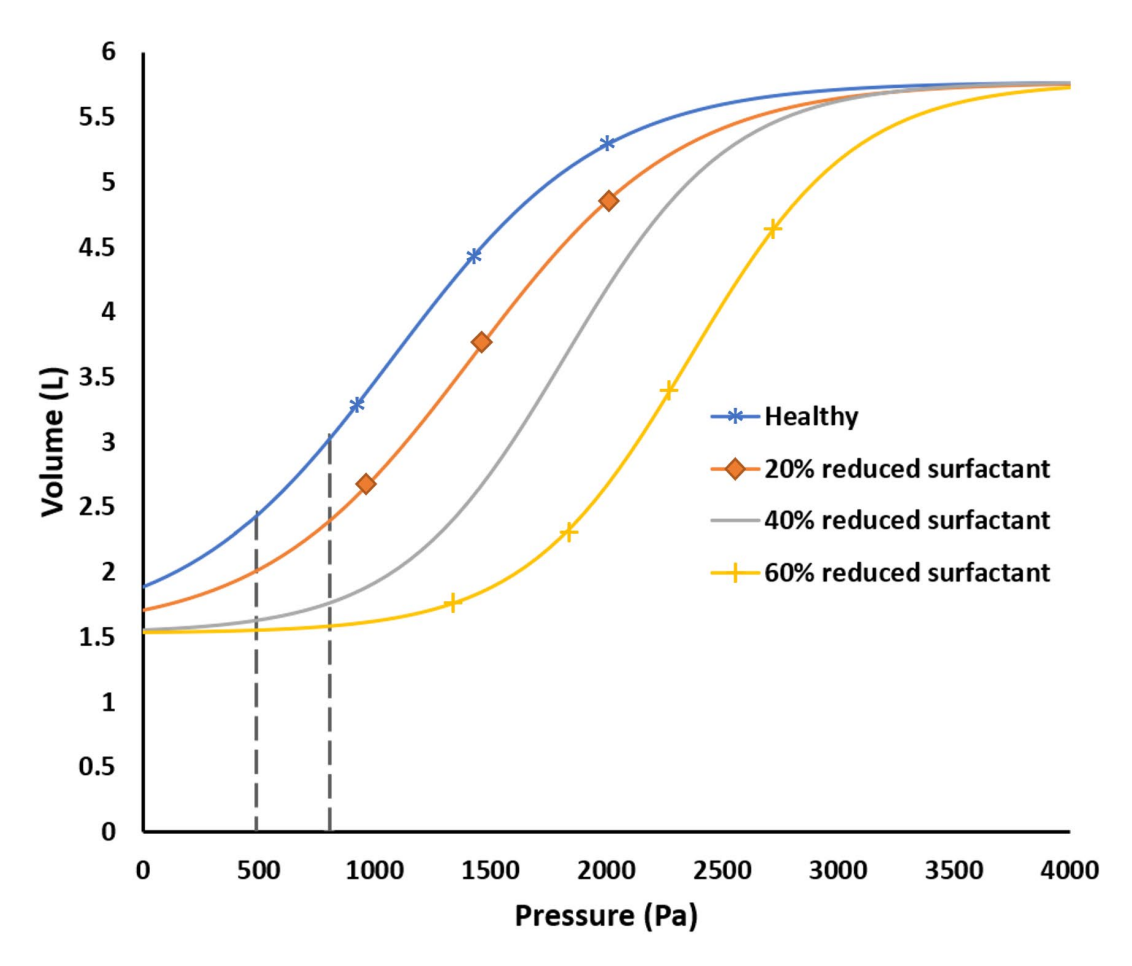


Figure 2: The sigmoidal model derived from [48] and [47] used in a simulation for healthy and COVID-19 affected lungs. The pressure – volume curve for a healthy lung is shown in blue. As damage progresses in the lungs, there is a progressive reduction of surfactant amount and compliance of the acinar units. The decrease in surfactant shifts the pressure-volume curves to the right, as seen in the 20% reduced surfactant (orange), 40% reduced surfactant (grey), and 60% reduced surfactant (yellow) cases. The dashed grey lines indicate the pressure range used for the simulation [51].

The MV waveform selected was based on the work of Dincel et al. [10] due to its similarity to shark-fin-shaped waveforms commonly used in MV. Our approach enabled comparison to the results of Szlavecz et al.'s [13] clinical study of MV, as well as to studies of MV based on this clinical trial, such as those by Morton et al. [12], [52]–[54]. Our

simulations used a PEEP of 5 cmH<sub>2</sub>O, a driving pressure (P<sub>C</sub>) of 10 cmH<sub>2</sub>O (and subsequent PIP of 15 cmH<sub>2</sub>O), an inspiration time ( $t_i$ ) of 0.5 seconds, a time constant ( $\tau_f$ ) of 0.075, an I:E ratio of 1:3, and a total respiratory period of 2 seconds/breath for a respiratory rate of 30 breaths per minute. COVID-19 and hypothetical healthy lungs subjected to MV were simulated for comparison.

# 3. Results

To qualitatively validate our simulation results, the output data from the model can be compared to output data from other MV studies. For example, Morton et al. [53] created virtual patients based on MV data from Szlavecz et al. [13]. This clinical trial from Szlavecz et al. [13] managed real-time patient respiratory mechanics with novel software connected to a volume-controlled ventilator. The authors noted that "[The volume-control] flow profile is similar to the flow profile generated during pressure control mode". Morton et al. [12], [54] used these flow profiles to generate a predictive model of MV. Figure 3 compares the flow output waveform from the Morton et al. [54] study to the flow output waveform from our research (for Subject 1). Note that the peak flow is considerably higher in the Morton et al. [54] waveform (approximately 6 L/s compared to our results of about 3.3 L/s in the healthy simulation), but the inspiratory period is also almost half as long as ours (approximately 0.25s in the Morton et al. [54] study and 0.5s in our study, which leads to similar tidal volumes. Thus, our study's general waveform appears to agree with the clinical and predictive models from Morton et al., despite using different input pressure waveforms [54].

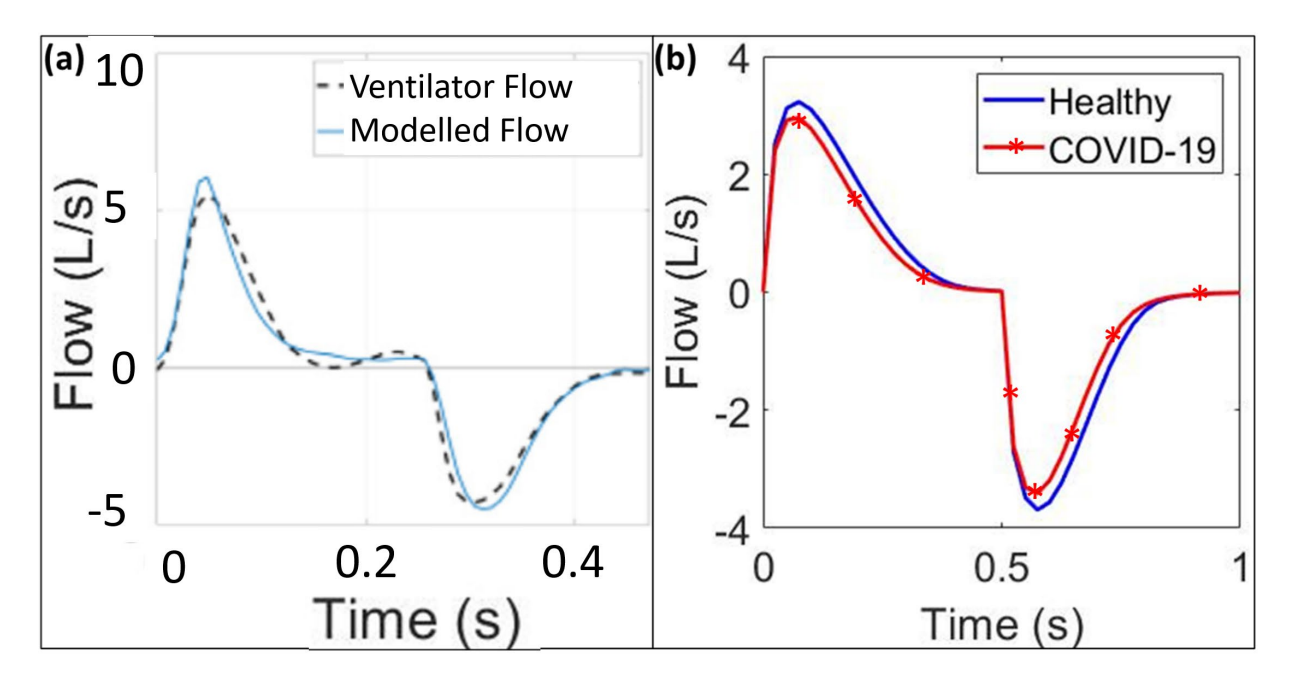
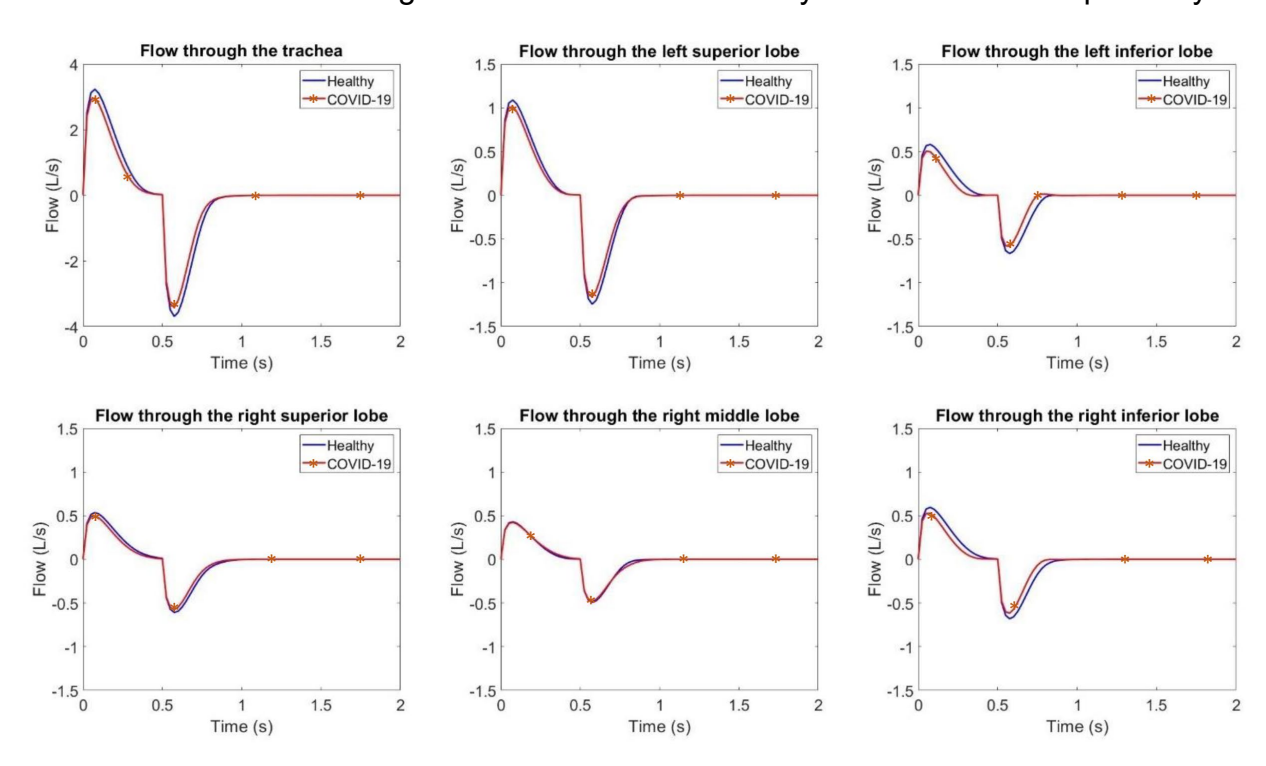


Figure 3: Flow waveform output from Morton et al. [54] (a) and the flow waveform output from simulation of Subject 1 at the trachea used in this study (b). The dashed line in (a) indicates clinical average results from a dataset of 14 patients. The solid line in (a) results from Morton's predictive model. (Image on the left is reprinted from Morton et al. [54] with permission from Elsevier)

Eight simulations were run in total for the four patients in this study: one of a hypothetical healthy lung subjected to MV and a COVID-19-afflicted simulation of MV for each subject. Figure 3 shows air flow rate at the trachea and into each lobe, determined by calculating the flow rate at the first airway branch that enters each lobe for a delivered breath. For Subject 1, airflow through the left lower lobe showed the largest reduction compared to the hypothetical healthy lung model due to the extensive damage present in this particular lobe. Flow rate was integrated over time to find the coincident change in the lung and lobar volumes, as shown in Figure 4 for Subject 1. As expected, the left lower lobe for Subject 1 demonstrated the largest reduction in air volume. All the plots for flow rate and volume over time results of the other three subjects are reported in Appendix A.

Tidal volumes reported in Figure 5 can be used to determine the lobar share of ventilation – the percentage of the tidal volume taken in by each lobe, for healthy and COVID-19 simulations. The percentage change of lobar share values of the healthy simulation to lobar share values of the COVID-19 simulation, are reported in Table 2 to examine the deviation between healthy and COVID-19 simulations quantitatively. The tidal volume differences between simulations demonstrate that if all simulation conditions are held the same other than the introduction of COVID-19 regions, flow and subsequent tidal volume within the lung will vary regionally (Figure 5). On average, the right middle lobe increased its lobar share by a substantial (9.4% - 20.5%) amount in COVID-19 cases, while the lobar share of the left and right lower lobes decreased by 12.8 and 7.3% respectively.



**Figure 4:** Flow through the trachea and individual lung lobes of Subject 1. The right middle lobe showed the least change in flow between the hypothetical healthy and COVID-19 simulations.

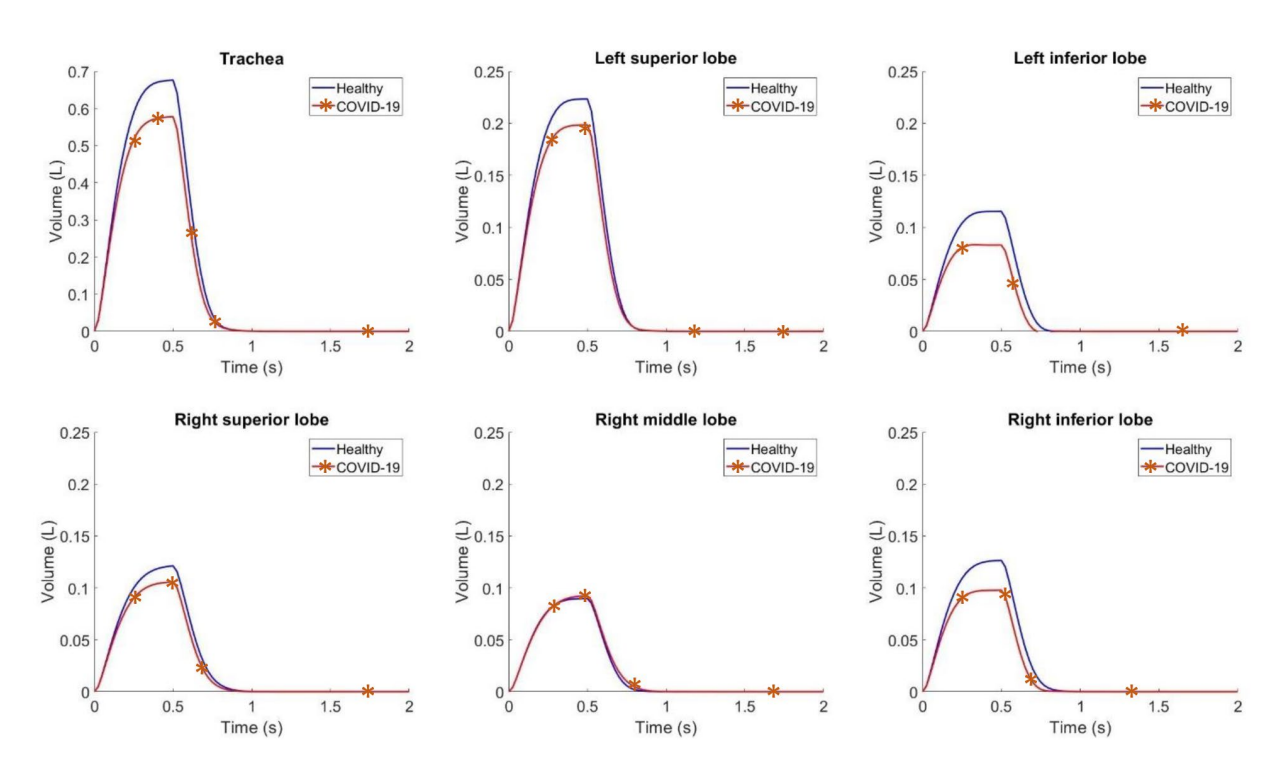


**Figure 5:** Volume of air passing through the trachea and individual lobes of Subject 1. The left lower lobe showed the largest reduction volume for the COVID-19 simulation compared to the hypothetical healthy case.

**Table 2:** Percent change in lobar share of ventilation between COVID-19 simulations and healthy simulations for each lobe of each subject. Negative values indicate a decrease in lobar share in the COVID-19 versus healthy simulation.

	Right upper	Right middle	Right lower	Left upper	Left lower
	lobe	lobe	lobe	lobe	lobe
Subject 1	2.1%	20.5%	-9.3%	4.0%	-15.5%
Subject 2	15.1%	9.4%	-11.4%	<b>-</b> 5.0%	-2.3%
Subject 3	4.9%	12.2%	8.8%	-0.8%	-19.3%
Subject 4	-4.8%	11.1%	-17.1%	12.8%	-13.9%
Average	4.3%	13.3%	-7.3%	2.8%	-12.8%

The COVID-19 afflicted percent, which is the percentage of the volume of each lobe that is affected by either GGOs or consolidation at end-inhalation based on the CT image, can be subtracted from the average COVID-19 affliction per lung to assess COVID-19 damage on a regional basis within each lung, as shown in Table 3. These values refer to how damaged a lobe is relative to the rest of the lung and will be referred to as the relative COVID-19 damage. On average, the right middle lobe was much healthier (>±10%) than the rest of the lung lobes for all subjects, while the right and left lower lobes were much more damaged than the rest of the lung.

**Table 3:** Difference between the average amount of COVID-19 damage within each lung and the COVID-19 damage within each lobe, derived from CT images. A positive value indicates that the lobe has more damage than average within that lung.

	Average	Relative COVID-19 damage					
	Average COVID-19 affected %	Right upper lobe	Right middle lobe	Right lower lobe	Left upper lobe	Left lower lobe	
Subject 1	57.3%	1.4%	-27.8%	20.9%	-12.2%	17.7%	
Subject 2	42.9%	-23.8%	-13.5%	21.8%	6.4%	9.0%	
Subject 3	48.2%	-5.8%	-10.4%	-10.9%	3.7%	23.5%	
Subject 4	55.3%	4.4%	-14.5%	13.4%	-18.9%	15.6%	
Average	50.9%	-5.9%	-16.6%	11.3%	-5.3%	16.5%	

Percentage change in lobar share of ventilation between healthy and COVID-19 simulations and relative COVID-19 damage per lobe can thus be compared to examine how air is redistributed in COVID-19 lungs, as shown in Figure 6. This figure illustrates the strong, nearly linear, negative dependence between relative COVID-19 lobar damage and lobar share of ventilation change. The Pearson correlation coefficient of the relationship was calculated in MATLAB R2019b (Mathworks Inc) as R = - 0.959 (fitting parameter  $R^2 = 0.9205$ ) with a p-value of  $2.45 \times 10^{-11}$ , allowing rejection of the null hypothesis  $\alpha = 5\%$  and indicating a significant, strongly negative, correlation. In other words, more healthy lung lobes tended to increase their share of ventilation, while less healthy lung lobes showed the tendency to decrease their ventilation share in our COVID-19 simulation as compared to our healthy simulation.

For instance in Table 3, note that for Subject 2, the right upper lobe with 19% COVID-19 damage, and right middle lobe with 29% COVID-19 involved are far healthier when compared to the average of 55% COVID-19 involvement for the other three lobes in this lung. The ventilation in the two healthier lobes increased relative to the other three lobes when the lung was subjected to COVID-19 (Table 2). This same trend of ventilatory redistribution occurred for all but one lobe (the left upper lobe in Subject 1). A Pearson correlation coefficient test was also completed for relative GGO damage and relative consolidation damage. Lobar share change was moderately negatively correlated (R = -0.750, p =  $1.40 \times 10^{-4}$ ) with relative GGO damage and strongly negatively correlated (R = -0.972, p =  $9.54 \times 10^{-13}$ ) with relative consolidation damage, suggesting that consolidation severity had a larger effect on redistribution than GGOs, but both caused a general decrease in the lobar share of ventilation.

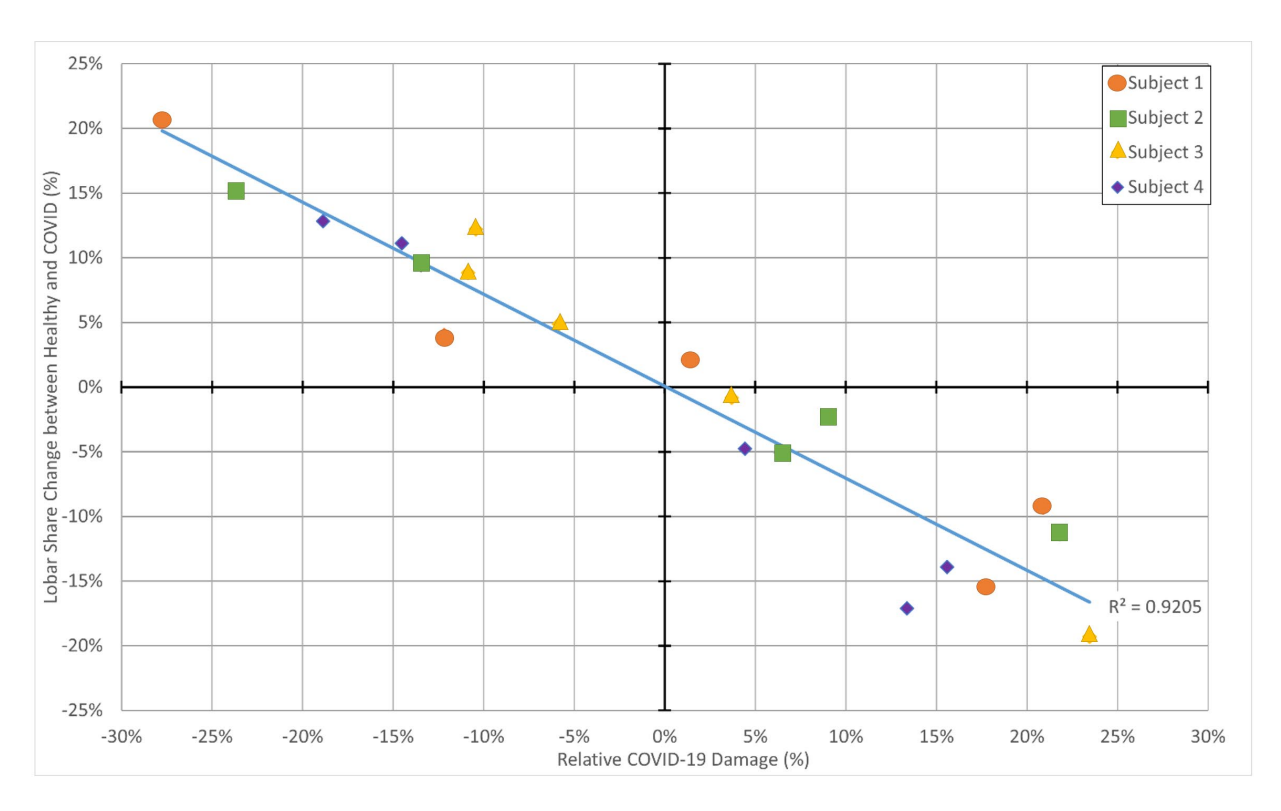


**Figure 6:** Relationship between lobar share of ventilation compared to the healthy case and relative COVID-19 damage for each lobe in all four patients, with a linear trendline and strong correlation (R<sup>2</sup> value) shown. more healthy lung lobes had the tendency to increase their share of ventilation while less healthy lung lobes showed the tendency to decrease their ventilation share in our COVID-19 simulation as compared to our healthy simulation.

Finally, respiratory static compliance, defined as the tidal volume delivered divided by the difference between PIP and PEEP, had an average value of  $63.9 \pm 8.6$  mL/cmH<sub>2</sub>O in healthy cases while the COVID-19 cases had an average of  $C_{RS} = 55.1 \pm 8.2$  mL/cmH<sub>2</sub>O, for a difference of -8.4 mL/cmH<sub>2</sub>O and a percent change of -13%. Depending on the subject, this percent change varied between -11.5% and -14.6%. To analyze the relationship between respiratory compliance and COVID-19 damage, pressure-volume curves were created for each lung and each lobe with the mechanical ventilator pressure output and tidal volume as variables. The P-V curves for Subject 1 are displayed in Figure 7, while the three sets of P-V curves for all other subjects can be found in the Appendix. The COVID-19 P-V loop shifted downward and to the right, indicating a lower tidal volume plateau. This is a signpost of decreased compliance, evidenced by the slope of each of these P-V curves. However, in healthier lobes, the downward shift was not as drastic.

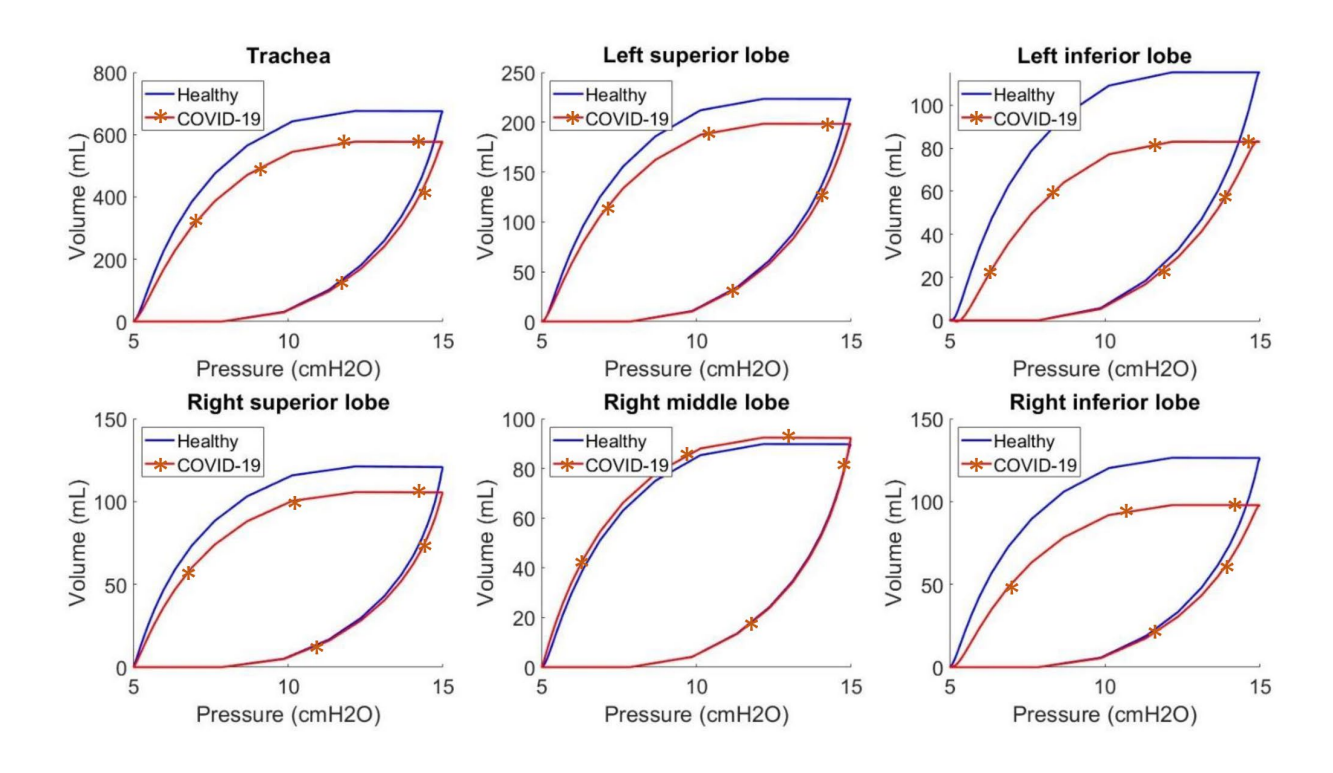


**Figure 7:** P-V curves for entire lung and each lobe for Subject 1, from hypothetical healthy and diseased lung MV simulations. The largest shifts in the P-V curve for the COVID-19 case can be seen in the right lower and left lower lobes.

### 4. Discussion

There is a need for high-fidelity image-based models of COVID-19 lungs to better understand and potentially improve MV outcomes. In this research, we developed a proofof-concept multi-scale image-based computational models of MV in COVID-19 patients and compared the results to a hypothetical healthy lung subjected to MV for comparison to demonstrate the potential of such image-based models in MV simualtion. Previously, Morton et al. authored a series of innovative studies [12], [52]-[54] on virtual patient models for the prediction of MV outputs. Similarly, Das et al. [11] proposed an in silico model of COVID-19 ARDS with a focus on MV. These models are complex and powerful, though they are not image-based, meaning they don't explicitly account for the lung and airway geometry and lobe-specific damage distribution in each patient. Image-based computational models, such as the one presented in this study, are computationally more expensive than the previously developed mathematical models, but nonetheless offer immense potential to be used in future virtual patient and cohort simulations for personalized treatment planning and MV protocol optimization [55]. Another drawback of image-based models is that they rely on the segmentation of clinical images, which can be labor-intensive. However, recent advances in automated CT segmentation using machine learning presents a potential solution to the tedious task manual image segmentation for model building.

Our study relied on a set of 4D CT images obtained from four patients with severe COVID-19 and exhibiting highly heterogenous damage distribution in the lung. The overall regional distribution of COVID-19 damage from the segmentation of CT images examined in this study agreed with previous studies. Within our cohort, the average COVID-19 damaged percentage (defined as the volume of COVID-19 affected region divided by total lung volume) at end-inhalation was 44% ± 16% in the right upper lobe, 33% ± 4% in the right middle lobe, 61% ± 15% in the right lower lobe, 45% ± 8% in the left upper lobe, and 66% ± 9% in the left lower lobe. Comparatively large standard deviations may be due to the small sample size of four in our study. In a screening of 120 chest CT scans of COVID-19 patients, Ahmadi et al. [56] estimated that the frequency of lobe involvement was 83% in the right upper, 70% in the right middle, 95% in the right lower, 80% in the left upper, and 92% in the left lower, while Bernheim et al. [57] estimated a similar frequency distribution (44%, 41%, 65%, 48%, and 63%, respectively) in a 121-patient cohort of CT scans where only 41% of patients presented with both GGOs and consolidation. Likewise, the literature supports the notion that COVID-19 damage occurs more frequently and with increased severity within the lower lobes [49], [58], [59]. This is indeed what is seen in our segmentation results, where the lower lobes were significantly more affected by GGO and consolidation damage than the upper or middle lobes. Additionally, COVID-19 affliction of larger than 10% of lobe volume was present in all twenty lobes of the four patients analyzed.

The COVID-19 lung simulations showed an overall reduction of 83.9 ± 9.0 mL in tidal volume when compared to the healthy simulation case with identical MV input, as anticipated based on the lower acinar compliance assigned to the COVID-19-infected lungs [47]. However, the COVID-19 lung models exhibited an average CRS of 55.1 ± 8.2 mL/cmH<sub>2</sub>O, a more minor reduction than observed in clinical settings and approximately 8.8 mL/cmH<sub>2</sub>O less than the simulated healthy value of 63.9 ± 8.6 mL/cmH<sub>2</sub>O. Bain et al. [60] calculated a CRS of 25-45 mL/cmH2O, and Grasseli et al. [61] estimated the CRS to be between 24-49 mL/cmH<sub>2</sub>O for mechanically ventilated CARDS, while other studies estimate a C<sub>RS</sub> between 24-53 mL/cmH<sub>2</sub>O for typical ARDS [36], [62]-[66]. Patients examined in these clinical MV settings are likely to have very severe COVID-19 damage and thus low compliance within damaged acini [67], [68]. COVID-19 damage may also be more widespread in severely ill patients' lungs. For instance, in a CT analysis of 21 severe CARDS patients, the average "poorly aerated" or "nonaerated" portion of the lung combined to approximately 70%, while the patients in our study only had an average poorly-aerated or non-aerated lung volume of about 51% [69]. Furthermore, the degree to which surfactant is reduced in COVID-19-infected acini has not been quantified, and our assumptions of 20% and 60% reduction in surfactant may be an underestimation of "severe" COVID-19 damage. Nevertheless, the results of this proof-of-concept study show a general reduction of static compliance within all lobes, as expected for COVID-19 lungs.

An interesting result of this study is related to ventilation redistribution between lobes in COVID-19-infected lungs under MV. Lobar share of ventilation was defined as the percentage of total tidal volume distributed to each lobe. Comparing the percentage change in lobar share of ventilation from healthy to COVID-19 simulation conditions revealed noticeable heterogeneity: on average, the right middle lobe of each lung

considerably increased its lobar share of ventilation in the COVID-19 simulation scenarios. In contrast, each lung's left and right lower lobes substantially decreased in the lobar share of ventilation in the COVID-19 simulation scenario. This indicates that the model is capable of simulating a general redistribution of ventilation: airflow increased, relatively, to the right middle lobes and declined in the lower lobes among the study's cohort. Thus, the simulation showed that, while subjected to MV, lobes of the lung less damaged by COVID-19 could see a relative increase in ventilation. In contrast, lobes more damaged by COVID-19 showed a relative reduction in ventilation (Figure 3). This heterogeneous distribution of COVID-19 damage and ventilation redistribution may offer new insights into the prevalence of ventilator-induced lung injury among COVID-19 patients. Particularly, healthy lung regions tend to have a higher propensity for expansion compared to edematous and damaged regions undergoing fibrosis in ARDS and CARDS- thus, MV may cause volutrauma in these more compliant healthy regions [70]. Note that in disease simulation scenario, tidal volumes in less damaged lobes never exceeded the corresponding healthy simulation tidal volumes, so one may assume that these lobes are not at risk of overdistention. While it may be true that this is unlikely to lead to considerable volutrauma, it should be noted that these diseased lobes are not healthy – they each have distinctly damaged portions – and cannot be treated as such. Therefore, when ventilation is redistributed into relatively healthier lobes, the COVID-19damaged portions of these lobes may also be subjected to increased flow. This can cause cyclic hyperinflation in these regions, and for less compliant (damaged) acini, localized volutrauma may have a compounding effect [71]-[73]. This is consistent with a clinical analysis by Cressoni et al. [74] that noted a substantial increase in mortality among ARDS patients with more inhomogeneous lung damage. However, increased volumetric strain is not the only cause of VILI; open alveoli surrounded by collapsed or fluid-filled alveoli can act as stress concentrators that can also cause damage during MV [75]. The increased heterogeneity of COVID-19 lung damage and ventilation, as demonstrated in CT images and simulation results, may lead to VILI due to the higher stress concentration imposed on the septal walls of neighboring healthier alveoli [75]. Moreover, as Perlman et al. [76] noted, these septal stress gradients between open and collapsed regions can increase the chance of VILI in lungs with highly heterogeneous damage, particularly if they also exhibit reduced surfactant (such as our COVID-19 acinar model). However, our model needs to be improved by incorporating a more realistic acinar geometry and interacinar interactions [77] to be able to simulate the aforementioned stress concentrations.

While this study models MV in COVID-19 lungs in a partially patient-specific manner in terms of the lobe and major airways geomtery, we also acknowledge our preliminary study's limitations. Even as the modeling workflow was demonstrated for four patients in the MV trial, validating the simulation results for a larger cohort of patients would allow for studying inter-subject variability of airflow. Additionally, all four patients analyzed here are male; future studies should include patients of both sexes. Furthermore, three out of four patients were classified as obese by BMI, and every patient was overweight. Obese subjects typically have lower FRC, tidal volume, and chest wall and lung compliance. As a result, they are not necessarily representative samples for modeling studies since data from CT may differ for patients with a healthy BMI [78]. Collateral ventilation, airway deformation [79], gas exchange [80], ventilation-perfusion modeling [81], realistic acinar geometries and alveolar ducts [82], none of which are implemented in this study, can also

affect the accuracy of the predicted airflow and pressure distributions and their incorporation in future iterations of the model can improve the fidelity of human lung digital twins [83]. Likewise, the lack of spirometry data and non-patient-specific chest wall compliance did not allow for the implementation of patient-specific boundary conditions and the direct validation of the model against 4DCT data [84]. Furthermore, a detailed sensitivity analysis of the model parameters needs to be performed in future studies to determine which parameters exert the most influence on the model's outputs.

Although surfactant dysfunction accounted for acinar level damage in this study, other forms of damage, such as diffuse alveolar wall damage, microangiopathy, edema, and fibrosis, lead to altered lung mechanics in the COVID-19-affected lung [85]. Including more detailed alveolar mechanics models and accounting for different types of damage explicitly in the simulations could further elucidate the impact of the disease on global lung function. Furthermore, our assumption of 20% reduced surfactant in GGOs, and 60% reduced surfactant, based on values by Fujioka et al. [47] for generally lower acinar compliance, is mainly arbitrary and may more accurately represent moderately damaged COVID-19 lungs than severely damaged ones. It would be beneficial to simulate a more advanced COVID-19 state in future studies, as it would be realistic for a patient with no independent breathing function. It should also be noted that increasing the degree of surfactant loss considerably increased the computational expense of our models due to larger pressure gradients.

The potential to use the preliminary model presented in this study is not limited to analysis of COVID-19 results, particularly if key study limitations can be overcome. For example, with a larger cohort, this approach could be used to establish predictive patient modeling, similar to that of Morton et al. [53] and the virtual trial of Ang et al. [86]. An image-based predictive model could offer new and more detailed insights into lung dynamics compared to data-driven predictive models. Another clinical application of the model would be in surfactant loss estimation. With access to spirometry data for a patient, this model could be run iteratively at different surfactant loss levels until results match the patient data, which would allow an estimation of the degree of surfactant loss [87]. Additionally, with increased computational power particularly using GPU-accelerated computing, many steps in this study can be automated for near-real-time high-fidelity modeling to better train medical students and inform clinicians. Finally, machine learning (ML) algorithms have recently gained traction as a powerful tool in MV interventions as reviewed recently by Baidillah et al. [88]. The combination of ML and computational image-based models may eventually make it possible to perform real-time patient-specific simulations and optimization of MV. As computer models accelerated by ML algorithms become more ubiquitous in simulation and optimization of MV, verification, validation and assessing the overall credibility of these models also takes front stage and needs increased attention [89], [90].

In conclusion, COVID-19 has caused worldwide death and disability since 2019 and continues to do so. Patients critically ill with severe COVID-19 are often treated with MV, which carries a risk of VILI. By investigating lung dynamics during MV for individual lobes, differences in lung geometry and mechanical behavior can be used to inform personalized MV treatment methods in the future. Therefore, this study presents a proof-of-concept modeling workflow to simulate the effect of heterogenous COVID-19-induced lung

damage on MV dynamics in a geometrically patient-specific manner. Hence, this modeling study lays the foundation for more complex patient-specific investigations of MV in COVID-19 patients and individualized treatment strategies.

#### **Declarations**

#### Ethics approval and consent to participate

The East Carolina University University and Medical Center Institutional Review Board (UMCIRB) approved the image collection and processing methodology used in this study with study ID 20-001447. Informed consent was obtained from each patient to participate in the study. The study was performed in accordance with the ethical standards as laid down in the 1964 Declaration of Helsinki and its later amendments or comparable ethical standards.

#### **Consent for publication**

Informed consent was obtained from each patient.

#### Availability of data and material

The datasets generated during and/or analyzed during the current study are available from the corresponding author on reasonable request.

#### Declarations of interest: none

#### **Funding**

This material is based on the work supported by the National Science Foundation under award # 2034964. This material is also based upon work supported by the National Science Foundation Graduate Research Fellowship under award # 2037785.

#### **Authors' contributions**

A.V., E.D., S. M., performed the method development and simulations and wrote the manuscript. M.S.P and A.J. collected the CT data. S.G. contributed to study conceptualization and manuscript revision, and V.M. contributed to protocol development. All authors reviewed the manuscript and contributed to the scientific discussion.

## **Acknowledgments**

The authors acknowledge support from Dr. Kaida Yang (Department of Radiation Oncology, East Carolina University).

### References

[1] J. L. Bernal *et al.*, "Effectiveness of Covid-19 Vaccines against the B.1.617.2 (Delta) Variant," https://doi.org/10.1056/NEJMoa2108891, Jul. 2021, doi: 10.1056/NEJMOA2108891.

- [2] N. Andrews *et al.*, "Covid-19 Vaccine Effectiveness against the Omicron (B.1.1.529) Variant," https://doi.org/10.1056/NEJMoa2119451, vol. 386, no. 16, pp. 1532–1546, Mar. 2022, doi: 10.1056/NEJMOA2119451.
- [3] J. H. Tanne, "Covid-19: BA.5 variant is now dominant in US as infections rise," *BMJ*, vol. 378, p. o1770, Jul. 2022, doi: 10.1136/BMJ.O1770.
- [4] P. G. Gibson, L. Qin, and S. H. Puah, "COVID-19 acute respiratory distress syndrome (ARDS): clinical features and differences from typical pre-COVID-19 ARDS," 2020, doi: 10.5694/mja2.50674.
- [5] E. Dimbath *et al.*, "Implications of microscale lung damage for COVID-19 pulmonary ventilation dynamics: A narrative review," *Life Sci*, p. 119341, Mar. 2021, doi: 10.1016/J.LFS.2021.119341.
- [6] C. Patte, "Personalized pulmonary mechanics: modeling, estimation and application to pulmonary fibrosis To cite this version: HAL Id: tel-03144413 Personalized pulmonary mechanics: modeling, estimation and application to pulmonary fibrosis," 2021.
- [7] J. N. Cronin, L. Camporota, F. Formenti, J. N. Correspondence, and L. Cronin, "Mechanical ventilation in COVID-19: A physiological perspective," *Exp Physiol*, 2021, doi: 10.1113/EP089400.
- [8] L. ZJ *et al.*, "Case Fatality Rates for Patients with COVID-19 Requiring Invasive Mechanical Ventilation. A Meta-analysis," *Am J Respir Crit Care Med*, vol. 203, no. 1, pp. 54–66, Jan. 2021, doi: 10.1164/RCCM.202006-2405OC.
- [9] R. S. P. Warnaar *et al.*, "Computational physiological models for individualised mechanical ventilation: a systematic literature review focussing on quality, availability, and clinical readiness," *Crit Care*, vol. 27, no. 1, Dec. 2023, doi: 10.1186/S13054-023-04549-9.
- [10] E. Dincel, "Advanced mechanical ventilation modes: design and computer simulations," https://doi.org/10.1080/10255842.2020.1845319, vol. 24, no. 6, pp. 673–686, 2020, doi: 10.1080/10255842.2020.1845319.
- [11] A. Das *et al.*, "In Silico Modeling of Coronavirus Disease 2019 Acute Respiratory Distress Syndrome: Pathophysiologic Insights and Potential Management Implications," *Crit Care Explor*, vol. 2, no. 9, p. e0202, 2020, doi: 10.1097/cce.0000000000000202.
- [12] S. E. Morton, "Development of Virtual Patients for use in Mechanical Ventilation," no. August, p. 186, 2019, [Online]. Available: http://hdl.handle.net/10092/17641
- [13] A. Szlavecz *et al.*, "The Clinical Utilisation of Respiratory Elastance Software (CURE Soft): a bedside software for real-time respiratory mechanics monitoring and mechanical ventilation management," *Biomed Eng Online*, vol. 13, no. 1, Sep. 2014, doi: 10.1186/1475-925X-13-140.
- [14] C. L. Lin, M. Tawhai, G. McLennan, and E. Hoffman, "Multiscale Simulation of Gas Flow in Subject-Specific Models of the Human Lung," *IEEE Engineering in Medicine and Biology Magazine*, vol. 28, no. 3, pp. 25–33, May 2009, doi: 10.1109/MEMB.2009.932480.

- [15] T. Gemci, V. Ponyavin, Y. Chen, H. Chen, and R. Collins, "Computational model of airflow in upper 17 generations of human respiratory tract," *J Biomech*, vol. 41, no. 9, pp. 2047–2054, Jan. 2008, doi: 10.1016/j.jbiomech.2007.12.019.
- [16] M. M. Ismail, Reduced Dimensional Modeling of the Entire Human Lung, vol. 19, no. 19. 2014.
- [17] M. Ismail, A. Comerford, and W. A. Wall, "Coupled and reduced dimensional modeling of respiratory mechanics during spontaneous breathing," *Int J Numer Method Biomed Eng*, vol. 29, no. July, pp. 1285–1305, 2013, doi: 10.1002/cnm.
- [18] A. J. Swan, A. R. Clark, and M. H. Tawhai, "A computational model of the topographic distribution of ventilation in healthy human lungs," *J Theor Biol*, vol. 300, p. 222, May 2012, doi: 10.1016/J.JTBI.2012.01.042.
- [19] Q. Sun, C. Zhou, and J. G. Chase, "Parameter updating of a patient-specific lung mechanics model for optimising mechanical ventilation," *Biomed Signal Process Control*, vol. 60, p. 102003, 2020, doi: 10.1016/j.bspc.2020.102003.
- [20] C. Zhou *et al.*, "Virtual patients for mechanical ventilation in the intensive care unit," *Comput Methods Programs Biomed*, vol. 199, p. 105912, 2021, doi: 10.1016/j.cmpb.2020.105912.
- [21] J. Kim and R. M. Pidaparti, "Computational Analysis of Lung and Isolated Airway Bifurcations under Mechanical Ventilation and Normal Breathing," *Fluids 2021, Vol. 6, Page 388*, vol. 6, no. 11, p. 388, Oct. 2021, doi: 10.3390/FLUIDS6110388.
- [22] R. Bordas *et al.*, "Development and analysis of patient-based complete conducting airways models," *PLoS One*, vol. 10, no. 12, pp. 1–20, 2015, doi: 10.1371/journal.pone.0144105.
- [23] K. Krishnan, L. Ibanez, W. D. Turner, J. Jomier, and R. S. Avila, "An open-source toolkit for the volumetric measurement of CT lung lesions," *Opt Express*, vol. 18, no. 15256, 2010.
- [24] A. Fedorov *et al.*, "3D Slicer as an image computing platform for the Quantitative Imaging Network," *Magn Reson Imaging*, vol. 30, no. 9, pp. 1323–1341, Nov. 2012, doi: 10.1016/j.mri.2012.05.001.
- [25] "3D Slicer image computing platform | 3D Slicer." https://www.slicer.org/ (accessed Jun. 29, 2021).
- [26] M. H. Tawhai, P. Hunter, J. Tschirren, J. Reinhardt, G. McLennan, and E. A. Hoffman, "CT-based geometry analysis and finite element models of the human and ovine bronchial tree," *J Appl Physiol*, vol. 97, no. 6, pp. 2310–2321, Dec. 2004, doi: 10.1152/japplphysiol.00520.2004.
- [27] M. H. Tawhai, A. J. Pullan, and P. J. Hunter, "Generation of an Anatomically Based Three-Dimensional Model of the Conducting Airways," 2000.
- [28] R. Bordas *et al.*, "Development and Analysis of Patient-Based Complete Conducting Airways Models," *PLoS One*, vol. 10, no. 12, p. e0144105, Dec. 2015, doi: 10.1371/journal.pone.0144105.
- [29] F. Cooper et al., "Chaste: Cancer, Heart and Soft Tissue Environment," J Open Source Softw, vol. 5, no. 47, p. 1848, Mar. 2020, doi: 10.21105/joss.01848.

- [30] J. E. McDonough, L. Knudsen, A. C. Wright, W. Mark Elliott, M. Ochs, and J. C. Hogg, "Regional differences in alveolar density in the human lung are related to lung height," *J Appl Physiol*, vol. 118, pp. 1429–1434, 2015, doi: 10.1152/japplphysiol.01017.2014.
- [31] R. Bordas *et al.*, "Development and Analysis of Patient-Based Complete Conducting Airways Models," *PLOS ONE*, vol. 10, no. 12, p. e0144105, Dec. 2015, doi: 10.1371/journal.pone.0144105.
- [32] M. H. Tawhai, P. Hunter, J. Tschirren, J. Reinhardt, G. McLennan, and E. A. Hoffman, "CT-based geometry analysis and finite element models of the human and ovine bronchial tree," *Journal of Applied Physiology*, vol. 97, no. 6, pp. 2310–2321, Dec. 2004, doi: 10.1152/japplphysiol.00520.2004.
- [33] R. Bumm, "First results of spatial reconstruction and quantification of COVID-19 chest CT infiltrates using lung CT analyzer and 3D slicer," *Br J Surg*, vol. 108, 2021.
- [34] M. T. Kassin *et al.*, "Generalized chest CT and lab curves throughout the course of COVID-19," *Scientific Reports 2021 11:1*, vol. 11, no. 1, pp. 1–13, Mar. 2021, doi: 10.1038/s41598-021-85694-5.
- [35] B. Chacko, J. V. Peter, P. Tharyan, G. John, and L. Jeyaseelan, "Pressure-controlled versus volume-controlled ventilation for acute respiratory failure due to acute lung injury (ALI) or acute respiratory distress syndrome (ARDS)," *Cochrane Database Syst Rev*, vol. 1, no. 1, Jan. 2015, doi: 10.1002/14651858.CD008807.PUB2.
- [36] J. M. Arnal, A. Garnero, M. Saoli, and R. L. Chatburn, "Parameters for Simulation of Adult Subjects During Mechanical Ventilation," *Respir Care*, vol. 63, no. 2, pp. 158–168, Feb. 2018, doi: 10.4187/RESPCARE.05775.
- [37] D. R. Hess, "Respiratory Mechanics in Mechanically Ventilated Patients," *Respir Care*, vol. 59, no. 11, pp. 1773–1794, Nov. 2014, doi: 10.4187/RESPCARE.03410.
- [38] L. Hao *et al.*, "Dynamic Characteristics of a Mechanical Ventilation System With Spontaneous Breathing," *IEEE Access*, vol. 7, pp. 172847–172859, 2019, doi: 10.1109/ACCESS.2019.2955075.
- [39] R. S. Harris, "Pressure-Volume Curves of the Respiratory System," *Respir Care*, vol. 50, no. 1, 2005.
- [40] H. G. Boren, R. C. Kory, and J. C. Syner, "The veterans administration-army cooperative study of pulmonary function. II. The lung volume and its subdivisions in normal men," *The American Journal of Medicine*, vol. 41, no. 1, pp. 96–114, 1966, doi: 10.1016/0002-9343(66)90008-8.
- [41] A. J. Swan, A. R. Clark, and M. H. Tawhai, "A computational model of the topographic distribution of ventilation in healthy human lungs," *J Theor Biol*, vol. 300, pp. 222–231, May 2012, doi: 10.1016/J.JTBI.2012.01.042.
- [42] M. M. Ismail, Reduced Dimensional Modeling of the Entire Human Lung, vol. 19, no. 19. 2014.
- [43] M. Ismail, A. Comerford, and W. A. Wall, "Coupled and reduced dimensional modeling of respiratory mechanics during spontaneous breathing," *Int J Numer Method Biomed Eng*, vol. 29, no. 11, pp. 1285–1305, Nov. 2013, doi: 10.1002/cnm.2577.

- [44] C. Van Ertbruggen, C. Hirsch, and M. Paiva, "Anatomically based three-dimensional model of airways to simulate flow and particle transport using computational fluid dynamics," *J Appl Physiol* (1985), vol. 98, no. 3, pp. 970–980, Mar. 2005, doi: 10.1152/JAPPLPHYSIOL.00795.2004.
- [45] T. A. Davis, "Algorithm 832," *ACM Transactions on Mathematical Software (TOMS)*, vol. 30, no. 2, pp. 196–199, Jun. 2004, doi: 10.1145/992200.992206.
- [46] T. A. Davis, "A column pre-ordering strategy for the unsymmetric-pattern multifrontal method," *ACM Transactions on Mathematical Software (TOMS)*, vol. 30, no. 2, pp. 165–195, Jun. 2004, doi: 10.1145/992200.992205.
- [47] H. Fujioka, D. Halpern, and D. P. Gaver, "A model of surfactant-induced surface tension effects on the parenchymal tethering of pulmonary airways," *J Biomech*, vol. 46, no. 2, pp. 319–328, Jan. 2013, doi: 10.1016/j.jbiomech.2012.11.031.
- [48] J. G. Venegas, R. Scott Harris, and B. A. Simon, "A comprehensive equation for the pulmonary pressure-volume curve," 1998, Accessed: Sep. 22, 2021. [Online]. Available: http://www.jap.org
- [49] E. Barisione *et al.*, "Fibrotic progression and radiologic correlation in matched lung samples from COVID-19 post-mortems," *Virchows Archiv*, vol. 478, no. 3, pp. 471–485, 2021, doi: 10.1007/s00428-020-02934-1.
- [50] S. Bayraktaroğlu, A. Çinkooğlu, N. Ceylan, and R. Savaş, "The novel coronavirus pneumonia (COVID-19): A pictorial review of chest CT features," *Diagnostic and Interventional Radiology*, vol. 27, no. 2, pp. 188–194, 2021, doi: 10.5152/dir.2020.20304.
- [51] S. Middleton *et al.*, "Towards a multi-scale computer modeling workflow for simulation of pulmonary ventilation in advanced COVID-19," *Comput Biol Med*, p. 105513, Apr. 2022, doi: 10.1016/J.COMPBIOMED.2022.105513.
- [52] S. E. Morton *et al.*, "A virtual patient model for mechanical ventilation," *Comput Methods Programs Biomed*, vol. 165, no. 2018, pp. 77–87, 2018, doi: 10.1016/j.cmpb.2018.08.004.
- [53] S. E. Morton *et al.*, "Predictive Virtual Patient Modelling of Mechanical Ventilation: Impact of Recruitment Function," 2019, doi: 10.1007/s10439-019-02253-w.
- [54] S. E. Morton et al., "Prediction of lung mechanics throughout recruitment maneuvers in pressure-controlled ventilation," Comput Methods Programs Biomed, vol. 197, p. 105696, 2020, doi: 10.1016/j.cmpb.2020.105696.
- [55] J. G. Chase *et al.*, "Next-generation, personalised, model-based critical care medicine: a state-of-the art review of in silico virtual patient models, methods, and cohorts, and how to validation them," *BioMedical Engineering OnLine 2018 17:1*, vol. 17, no. 1, pp. 1–29, Feb. 2018, doi: 10.1186/S12938-018-0455-Y.
- [56] J. Ahmadi *et al.*, "Evaluation of chest CT scan finding in the patients with acute respiratory symptoms following positive results of RT-PCR-COVID19," *Int J Physiol Pathophysiol Pharmacol*, vol. 14, no. 1, p. 48, 2022, Accessed: May 29, 2022. [Online]. Available: /pmc/articles/PMC8918605/

- [57] A. Bernheim *et al.*, "Chest CT findings in coronavirus disease 2019 (COVID-19): Relationship to duration of infection," *Radiology*, vol. 295, no. 3, pp. 685–691, Jun. 2020, doi: 10.1148/RADIOL.2020200463/ASSET/IMAGES/LARGE/RADIOL.2020200463.FIG5B.JPEG.
- [58] F. Shan *et al.*, "Lung Infection Quantification of COVID-19 in CT Images with Deep Learning Author list".
- [59] F. Song *et al.*, "Emerging 2019 Novel Coronavirus (2019-nCoV) Pneumonia," *Radiology*, vol. 297, no. 3, p. E346, Dec. 2020, doi: 10.1148/RADIOL.2020209021.
- [60] W. Bain *et al.*, "COVID-19 versus Non–COVID-19 Acute Respiratory Distress Syndrome: Comparison of Demographics, Physiologic Parameters, Inflammatory Biomarkers, and Clinical Outcomes," *Ann Am Thorac Soc*, vol. 18, no. 7, pp. 1202–1210, 2021, doi: 10.1513/AnnalsATS.202008-1026OC.
- [61] G. Grasselli *et al.*, "Mechanical ventilation parameters in critically ill COVID-19 patients: a scoping review," *Crit Care*, vol. 25, no. 1, Dec. 2021, doi: 10.1186/S13054-021-03536-2.
- [62] F. Fusina *et al.*, "Respiratory system compliance at the same PEEP level is similar in COVID and non-COVID ARDS," *Respir Res*, vol. 23, no. 1, pp. 1–8, Dec. 2022, doi: 10.1186/S12931-022-01930-0/FIGURES/3.
- [63] K. E. Swenson and E. R. Swenson, "Pathophysiology of Acute Respiratory Distress Syndrome and COVID-19 Lung Injury," *Crit Care Clin*, vol. 37, no. 4, pp. 749–776, Oct. 2021, doi: 10.1016/J.CCC.2021.05.003.
- [64] C. Brault *et al.*, "COVID-19- versus non-COVID-19-related acute respiratory distress syndrome: Differences and similarities," *Am J Respir Crit Care Med*, vol. 202, no. 9, pp. 1301–1304, Nov. 2020, doi: 10.1164/RCCM.202005-2025LE/SUPPL\_FILE/DISCLOSURES.PDF.
- [65] S. G. L. H. Nijbroek et al., "Low tidal volume ventilation is associated with mortality in COVID-19 patients—Insights from the PRoVENT-COVID study," J Crit Care, vol. 70, p. 154047, Aug. 2022, doi: 10.1016/J.JCRC.2022.154047.
- [66] L. Roesthuis, M. Van Den Berg, and H. Van Der Hoeven, "Advanced respiratory monitoring in COVID-19 patients: use less PEEP!," *Crit Care*, vol. 24, no. 1, 2020, doi: 10.1186/S13054-020-02953-Z.
- [67] M. Mahendra, A. Nuchin, R. Kumar, S. Shreedhar, and P. A. Mahesh, "Predictors of mortality in patients with severe COVID-19 pneumonia a retrospective study," *Adv Respir Med*, vol. 89, no. 2, pp. 135–144, Apr. 2021, doi: 10.5603/ARM.A2021.0036.
- [68] Y. Wang, Y. Wang, Y. Chen, and Q. Qin, "Unique epidemiological and clinical features of the emerging 2019 novel coronavirus pneumonia (COVID-19) implicate special control measures," *J Med Virol*, vol. 92, no. 6, pp. 568–576, Jun. 2020, doi: 10.1002/JMV.25748.
- [69] T. Fossali *et al.*, "Effects of Prone Position on Lung Recruitment and Ventilation-Perfusion Matching in Patients With COVID-19 Acute Respiratory Distress Syndrome: A Combined CT Scan/Electrical Impedance Tomography Study," *Crit Care Med*, vol. 50, no. 5, May 2022, doi: 10.1097/CCM.000000000005450.

- [70] J. J. Marini, P. R. M. Rocco, and L. Gattinoni, "CONCISE CLINICAL REVIEW Static and Dynamic Contributors to Ventilator-induced Lung Injury in Clinical Practice Pressure, Energy, and Power," 2020, doi: 10.1164/rccm.201908-1545CI.
- [71] D. P. Gaver, G. F. Nieman, L. A. Gatto, M. Cereda, N. M. Habashi, and J. H. T. Bates, "The POOR get POORer: A hypothesis for the pathogenesis of ventilator-induced lung injury," *Am J Respir Crit Care Med*, vol. 202, no. 8, pp. 1081–1087, Oct. 2020, doi: 10.1164/RCCM.202002-0453CP/SUPPL\_FILE/DISCLOSURES.PDF.
- [72] F. Cipulli, F. Vasques, E. Duscio, F. Romitti, M. Quintel, and L. Gattinoni, "Atelectrauma or volutrauma: the dilemma," *J Thorac Dis*, vol. 10, no. 3, p. 1258, Mar. 2018, doi: 10.21037/JTD.2018.02.71.
- [73] J. H. T Bates, D. P. Gaver, N. M. Habashi, and G. F. Nieman, "Critical Care Explorations Critical Care Explorations Atelectrauma Versus Volutrauma: A Tale of Two Time-Constants," 2020, doi: 10.1097/CCE.000000000000299.
- [74] M. Cressoni et al., "Lung Inhomogeneity in Patients with Acute Respiratory Distress Syndrome," https://doi.org/10.1164/rccm.201308-1567OC, vol. 189, no. 2, pp. 149–158, Jan. 2014, doi: 10.1164/RCCM.201308-1567OC.
- [75] G. F. Nieman *et al.*, "Physiology in Medicine: Understanding dynamic alveolar physiology to minimize ventilator-induced lung injury," https://doi.org/10.1152/japplphysiol.00123.2017, vol. 122, no. 6, pp. 1516–1522, Jun. 2017, doi: 10.1152/JAPPLPHYSIOL.00123.2017.
- [76] C. E. Perlman, "The Contribution of Surface Tension-Dependent Alveolar Septal Stress Concentrations to Ventilation-Induced Lung Injury in the Acute Respiratory Distress Syndrome," *Front Physiol*, vol. 11, p. 388, Jun. 2020, doi: 10.3389/FPHYS.2020.00388/BIBTEX.
- [77] C. J. Roth, M. Ismail, L. Yoshihara, and W. A. Wall, "A comprehensive computational human lung model incorporating inter-acinar dependencies: Application to spontaneous breathing and mechanical ventilation," *Int J Numer Method Biomed Eng*, vol. 33, no. 1, p. e02787, Jan. 2017, doi: 10.1002/cnm.2787.
- [78] A. E. Dixon and U. Peters, "The effect of obesity on lung function," *Expert Rev Respir Med*, vol. 12, no. 9, p. 755, Sep. 2018, doi: 10.1080/17476348.2018.1506331.
- [79] A. J. Swan, A. R. Clark, and M. H. Tawhai, "A computational model of the topographic distribution of ventilation in healthy human lungs," *J Theor Biol*, vol. 300, pp. 222–231, May 2012, doi: 10.1016/j.jtbi.2012.01.042.
- [80] L. J. Caucha, S. Frei, and O. Rubio, "Finite element simulation of fluid dynamics and CO 2 gas exchange in the alveolar sacs of the human lung," *Computational and Applied Mathematics*, vol. 37, no. 5, pp. 6410–6432, Nov. 2018, doi: 10.1007/s40314-018-0692-5.
- [81] B. Shaarbaf Ebrahimi *et al.*, "A computational model of contributors to pulmonary hypertensive disease: impacts of whole lung and focal disease distributions," *Pulm Circ*, vol. 11, no. 4, pp. 1–15, 2021, doi: 10.1177/20458940211056527.

- [82] E. Denny and R. C. Schroter, "Viscoelastic Behavior of a Lung Alveolar Duct Model," 2000. Accessed: Jun. 16, 2020. [Online]. Available: https://asmedigitalcollection.asme.org/biomechanical/article-pdf/122/2/143/5766987/143\_1.pdf
- [83] A. R. Clark, K. S. Burrowes, and M. H. Tawhai, "Ventilation/Perfusion Matching: Of Myths, Mice, and Men," *Physiology (Bethesda)*, vol. 34, no. 6, pp. 419–429, Nov. 2019, doi: 10.1152/PHYSIOL.00016.2019.
- [84] A. R. Clark and M. H. Tawhai, "Temporal and spatial heterogeneity in pulmonary perfusion: A mathematical model to predict interactions between macro-and micro-vessels in health and disease," *ANZIAM Journal*, vol. 59, no. 4, pp. 562–580, Apr. 2018, doi: 10.1017/S1446181118000111.
- [85] C. Van Ertbruggen, C. Hirsch, and M. Paiva, "Anatomically based three-dimensional model of airways to simulate flow and particle transport using computational fluid dynamics," *J Appl Physiol* (1985), vol. 98, no. 3, pp. 970–980, Mar. 2005, doi: 10.1152/JAPPLPHYSIOL.00795.2004.
- [86] C. Y. S. Ang *et al.*, "Virtual patient framework for the testing of mechanical ventilation airway pressure and flow settings protocol," *Comput Methods Programs Biomed*, vol. 226, Nov. 2022, doi: 10.1016/J.CMPB.2022.107146.
- [87] S. Piva et al., "Surfactant therapy for COVID-19 related ARDS: a retrospective case—control pilot study," Respir Res, vol. 22, no. 1, pp. 1–8, Dec. 2021, doi: 10.1186/S12931-020-01603-W/TABLES/3.
- [88] M. R. Baidillah, P. Busono, and R. Riyanto, "Mechanical ventilation intervention based on machine learning from vital signs monitoring: a scoping review," *MeScT*, vol. 34, no. 6, p. 062001, Jun. 2023, doi: 10.1088/1361-6501/ACC11E.
- [89] "Federal Register :: Assessing the Credibility of Computational Modeling and Simulation in Medical Device Submissions; Draft Guidance for Industry and Food and Drug Administration Staff; Availability." https://www.federalregister.gov/documents/2021/12/23/2021-27812/assessing-the-credibility-of-computational-modeling-and-simulation-in-medical-device-submissions (accessed Jul. 18, 2023).
- [90] G. Bideault, A. Scaccia, T. Zahel, R. W. Landertinger, and C. Daluwatte, "Verification and Validation of Computational Models Used in Biopharmaceutical Manufacturing: Potential Application of the ASME Verification and Validation 40 Standard and FDA Proposed Al/ML Model Life Cycle Management Framework," *J Pharm Sci*, vol. 110, no. 4, pp. 1540–1544, Apr. 2021, doi: 10.1016/J.XPHS.2021.01.016.